# Rational construction of three dimensional hybrid $Co_3O_4$@$NiMoO_4$ nanosheets array for energy storage application

Wei Hong [a, b], Jinqing Wang [a, *], Peiwei Gong [a, b], Jinfeng Sun [a, b], Lengyuan Niu [a, b], Zhigang Yang [a], Zhaofeng Wang [a], Shengrong Yang [a, *]

[a] State Key Laboratory of Solid Lubrication, Lanzhou Institute of Chemical Physics, Chinese Academy of Sciences, Lanzhou 730000, PR China
[b] University of Chinese Academy of Sciences, Beijing 100080, PR China

## HIGHLIGHTS

- $Co_3O_4$ NSA can be prepared through a facile chemical etching assistant approach.
- Rational designed 3D hybrid $Co_3O_4$@$NiMoO_4$ has been successfully constructed.
- The hybrid $Co_3O_4$@$NiMoO_4$ shows enhanced pseudocapacitive properties.

## ARTICLE INFO

## ABSTRACT

Electrodes with rationally designed hybrid nanostructures can offer many opportunities for the enhanced performance in electrochemical energy storage. In this work, the uniform 2D $Co_3O_4$-based building blocks have been prepared through a facile chemical etching assistant approach and a following treatment of thermal annealing. The obtained nanosheets array has been directly employed as 2D backbone for the subsequent construction of hybrid nanostructure of $Co_3O_4$@$NiMoO_4$ by a simple hydrothermal synthesis. As a binder-free electrode, the constructed 3D hybrid nanostructures exhibit a high specific capacitance of 1526 F $g^{-1}$ at a current density of 3 mA $cm^{-2}$ and a capacitance retention of 72% with the increase of current density from 3 mA $cm^{-2}$ to 30 mA $cm^{-2}$. Moreover, an asymmetric supercapacitor based on this hybrid $Co_3O_4$@$NiMoO_4$ and activated carbon can deliver a maximum energy density of 37.8 Wh $kg^{-1}$ at a power density of 482 W $kg^{-1}$. The outstanding electrochemical behaviors presented here suggest that this hybrid nanostructured material has potential applications in energy storage.

## 1. Introduction

Over the past decades, the growing demand for renewable sources has largely triggered the worldwide research on electrical energy storage devices (EES). As one of the promising candidates for energy storage, supercapacitors (SCs) have been paid great attention due to their excellent properties such as high power density, fast recharge capability and long cycle life [1]. Generally, pseudo-capacitors based on transition metal oxides can offer higher capacitance values than carbon materials based electrochemical double-layer capacitors (EDLs) [2]. Therefore, tremendous efforts have been focused on the former type of supercapacitors [3–6].

In order to obtain high-performance of pseudo-capacitors, the structural improvement based on the electrode materials is largely requisite [7–12]. Exploring proper nanomaterials, especially rationally designed three-dimensional (3D) metal oxide hybrid nanostructures (usually, fabricated by certain 1D or/and 2D building blocks), has always been an attractive topic [13–20]. Among various low-dimensional metal oxide building blocks, Co-based nanosheets array has been considered as one of promising electrode materials due to its high theoretical capacitance, environment benignity and good pseudo-capacitive performance in alkaline solutions [21–24]. Up to now, the synthesis of metal oxide nanosheets array can be generally actualized by two approaches: electro-deposition and hydrothermal synthesis [25–32]. In contrast to electro-deposition, active materials obtained by hydrothermal synthesis can provide uniform and large-scale nanosheets array with numerous large channels, which would facilitate

* Corresponding authors. Tel.: +86 931 4968076; fax: +86 931 8277088.
  E-mail addresses: jqwang@licp.cas.cn (J. Wang), sryang@licp.cas.cn (S. Yang).

the design and fabrication of 3D hybrid nanostructures [21,22,24,25,33]. However, regardless of the type of electrode materials, the capacitance values of 2D building blocks obtained by hydrothermal synthesis are still limited [33−37]. Therefore, it will be meaningful to explore an efficient assistant method to prepare large-scale 2D nanosheets array with the improved pseudo-capacitive performance.

As an attractive member in the class of the $AMoO_4$ type materials, $NiMoO_4$ has attracted more and more research interest due to its potential application in electrical energy storage [38,39]. However, the researches on its nanostructure fabrication and pseudo-capacitive performances have been rarely referred to [40,41]. To date, the reported electrode materials based on $NiMoO_4$ have been usually made by a traditional slurry-coating method, where the involved carbon current collector and polymer binders (or additives) can seriously depress the pseudo-capacitive performance [42−46]. In order to meet the requirement of higher capacitance values, one promising method is to fabricate smartly designed hybrid nanostructures combined with other uniformly low-dimensional building blocks [47,48].

In the present work, we have prepared uniform 2D $Co_3O_4$-based building blocks through a facile chemical etching assistant approach, and used this to construct a binder-free electrode with hybrid nanostructured $Co_3O_4@NiMoO_4$ directly grown on Ni foam. The electrochemical tests showed that this as-synthesized 3D $Co_3O_4@NiMoO_4$ electrode exhibited a high specific capacitance of 1526 F g$^{-1}$ at 3 mA cm$^{-2}$, and excellent rate performance (72% capacity retention at 30 mA cm$^{-2}$). To further evaluate the practical application of this hybrid $Co_3O_4@NiMoO_4$ NSA in EES, an asymmetric supercapacitor (AS) was also fabricated. The as-fabricated AS achieved a specific capacitance of 121 F g$^{-1}$ at a current density of 5 mA cm$^{-2}$, and a maximum energy density of 37.8 Wh kg$^{-1}$ at a power density of 482 W kg$^{-1}$. Such attractive electrochemical performance presented here implies that this hybrid electrode can be a promising candidate for practical applications in supercapacitor.

## 2. Experimental section

### 2.1. Preparation of uniform 2D $Co_3O_4$ nanosheets array

The approach for synthesizing uniform 2D $Co_3O_4$-based nanosheets array (NSA) has employed the CoAl layered double hydroxides (CoAl LDH) as pristine material, and the CoAl LDH NSA was synthesized by a simple homogeneous hydrothermal method [49−51]. Typically, the reaction solution was obtained by mixing $Co(NO_3)_2 \cdot 6H_2O$ (1 mmol), $Al(NO_3)_3 \cdot 9H_2O$ (0.5 mmol), $NH_4F$ (5 mmol), and urea (35 mmol) in 50 mL of ultrapure water with $n(Co)/n(Al) = 2:1$. After being stirred for 1 h, the homogeneous pink solution was transferred into a Teflon-lined stainless steel autoclave, and then a piece of Ni foam was immersed into the reaction solution. Subsequently, the bottle was capped and maintained at 95 °C for 6 h in an electric oven and then cooled down to room temperature. After the reaction, the sample was collected and rinsed several times with ultrapure water. The as-prepared precursor on the Ni foam was directly immersed in 5 M NaOH for chemical etching overnight, and then rinsed several times by ultrapure water [52,53]. Finally, the uniform 2D $Co_3O_4$-based NSA was obtained by annealing at 300 °C for 3 h. For comparison, the sample of CoAl layered double oxides (CoAl LDO) was also prepared under the same annealing conditions.

### 2.2. Preparation of $Co_3O_4@NiMoO_4$ hybrid nanostructures

To obtain hybrid nanostructures of $Co_3O_4@NiMoO_4$, the subsequent hydrothermal growth of $NiMoO_4$ was processed in 50 mL aqueous solution containing 0.5 M $Ni(CH_3COO)_2 \cdot 4H_2O$ and 0.5 M

$Na_2MoO_4 \cdot 7H_2O$ [38,41,46]. The chemical-etched CoAl LDH NSA (before annealing treatment) was directly immersed in the aforementioned reaction solution. The reaction was processed at 140 °C for 1 h. After that, the sample was collected and rinsed several times with ultrapure water. For comparison, the aforementioned solution was further used to fabricate other $Co_3O_4@NiMoO_4$ samples with the reaction times of 0.5 h and 2 h, respectively. Finally, the Ni foam with the as-prepared hydrate precursors was annealed at 300 °C for 3 h to obtain hybrid $Co_3O_4@NiMoO_4$.

### 2.3. Material characterizations and electrochemical measurements

X-ray diffraction (XRD) patterns were recorded on a Rigaku XRD-2400 diffractometer, using Cu-Kα radiation at 40 kV and 60 mA. The nanostructured samples were observed by using a field emission scanning electron microscope (FESEM, JSM-6701F) and a field emission transmission electron microscope (FETEM, TF20). X-ray photoelectron spectroscopy (XPS) was carried out by using ESCALAB 210 spectrometer (VG Scientific, UK). Nitrogen adsorption/desorption isotherms were measured on an asap 2020 analyzer. All samples were out gassed at 80 °C for 6 h under vacuum prior to measurements. The specific surface areas were calculated using the Brunauer−Emmett−Teller (BET) method.

The electrochemical measurements were carried out in a three-electrode electrochemical cell by using the CHI 660E Electrochemical Workstation at room temperature with the 2 M KOH as the electrolyte. The Ni foam supported active materials ($Co_3O_4$-based NSA mass ≈ 0.8 mg cm$^{-2}$, CoAl LDO NSA mass ≈ 1.1 mg cm$^{-2}$, $Co_3O_4@NiMoO_4$ NSA mass ≈ 1.75 mg cm$^{-2}$) were used directly as the working electrodes. A Pt plate and an SCE electrode were used as the counter electrode and the reference electrode, respectively. Electrochemical impedance spectroscopy (EIS) tests were conducted by using a perturbation amplitude of 5 mV in the frequency range from 0.01 Hz to 100 kHz. The galvanostatic charge/discharge tests were conducted on a LAND battery program-control test system. The mass-specific capacitance (MSC, $C_s$) [F g$^{-1}$] and areal-specific capacitance (ASC, $C_a$) [F cm$^{-2}$] were calculated from the galvanostatic discharge curves using equations as below:

$$C_s = It/m\Delta V$$

$$C_a = It/S\Delta V$$

where $I$ represents the charge−discharge current (A), $t$ is the discharge time (s), $\Delta V$ is the potential (V), $S$ is the geometrical area of the electrode, and $m$ designates the total mass of the active materials (g) [13,16,20].

### 2.4. Fabrication of the asymmetric supercapacitor

The electrochemical performances of asymmetric supercapacitor (AS) were explored under a two-electrode cell in 2 M KOH electrolyte solution [3]. The as-synthesized $Co_3O_4@NiMoO_4$ NSA on Ni foam was directly used as positive electrode, and the activated carbon (AC) was used as negative electrode. The negative electrode was prepared by a traditional "slurry-coating" method, and the similar process can be found in the references [44,61]. The charge balance between the two electrodes will follow the relationship $q^+ = q^-$. The charge stored ($q$) by each electrode depends on the following equation:

$$q = mC\Delta V$$

where $C$ represents the specific capacitance of the electrode (F g$^{-1}$), $\Delta V$ is the potential (V), and $m$ designates the total mass of the active
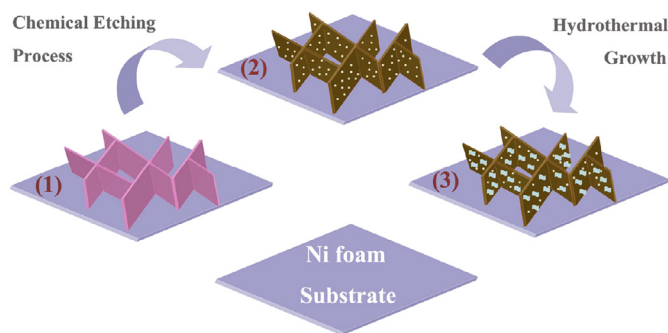
**Scheme 1.** Schematic illustration of the chemical etched synthesis of hybrid $Co_3O_4$@$NiMoO_4$ NSA electrode.

materials ($g$). To get $q^+ = q^-$, the mass ratio between the positive and negative electrodes needs to follow [42]:

$$m_+/m_- = \Delta V_- C_- / \Delta V_+ C_+$$

The energy density ($E$) and power density ($P$) were also calculated as follows [3,43]:

$$E = 0.5 C (\Delta V)^2$$

$$P = E/t$$

## 3. Results and discussion

As shown in Scheme 1, the construction of hybrid $Co_3O_4$@$NiMoO_4$ nanostructure as a binder-free electrode involves two key steps. First, CoAl LDH NSA was employed as precursor for preparing

the uniform 2D $Co_3O_4$-based NSA through chemical etching process. Second, the chemical-etched sample without thermal annealing was directly immersed in the reaction solution for the further hydrothermal growth of $NiMoO_4$.

Fig. 1 displays the XRD patterns of the chemical etched $Co_3O_4$ NSA and hybrid $Co_3O_4$@$NiMoO_4$ NSA, respectively. Apparently, the three highest intensity peaks located at 44.4, 51.6, and 76.1° in both patterns can be indexed to (111), (200), and (220) of metallic nickel, respectively [3,24,54]. The reflection peaks beside the Ni foam for the chemical etched $Co_3O_4$ NSA electrode belong to $Co_3O_4$ (JCPDS no. 42-1467), which is consistent with the previous reports [48]. For the $Co_3O_4$@$NiMoO_4$ NSA, two weak peaks at 19.3 and 49.3° belong to the $NiMoO_4$ (JCPDS no. 33-0948), demonstrating that the existence of α-$NiMoO_4$ in the hybrid composite [55]. Besides, the similar XRD results based on powder samples can be found in Fig. S1, which was carried out by scraping the active materials from Ni foam before tests. The surface chemical composition of the hybrid sample can be further verified by XPS, as shown in Fig. 1B–D. The Co 2p core level spectrum shows two speaks with binding energies of 781 and 796 eV, representing the Co $2p_{3/2}$ and Co $2p_{1/2}$ for $Co_3O_4$, respectively. The Ni 2p core level XPS spectrum shows two major peaks at 856 and 873.8 eV, which can be assigned to Ni $2p_{3/2}$ and Ni $2p_{1/2}$, representative of the existence of the $Ni^{2+}$. Two binding energy peaks located at 232.6 and 235.7 eV can be observed in the region of Mo 3d, which is a signature of $Mo^{6+}$ oxidation state [39].

Morphologies of the CoAl LDO NSA and the bare $Co_3O_4$-based NSA were observed by SEM. As shown in Fig. 2, the SEM images reveal that the uniform films of the two samples on the Ni foam are composed of regular nanosheets, and these films grow vertically and have an open-up network structures covered uniformly on the substrate surface. After the chemical etching process, the covered film of the bare $Co_3O_4$-based NSA still preserves the unique
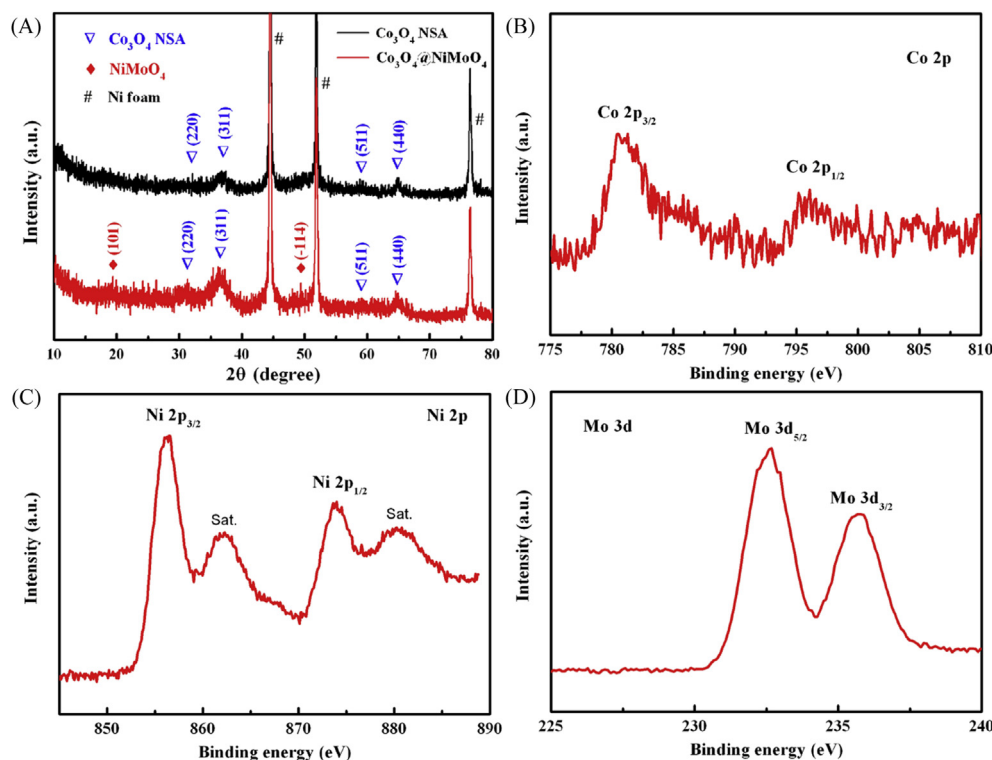


**Fig. 1.** (A) XRD patterns of the chemical etched $Co_3O_4$ NSA and hybrid $Co_3O_4$@$NiMoO_4$ NSA electrodes. (B, C, D) XPS spectra of Co 2p, Ni 2p and Mo 3d for hybrid $Co_3O_4$@$NiMoO_4$ NSA electrode.
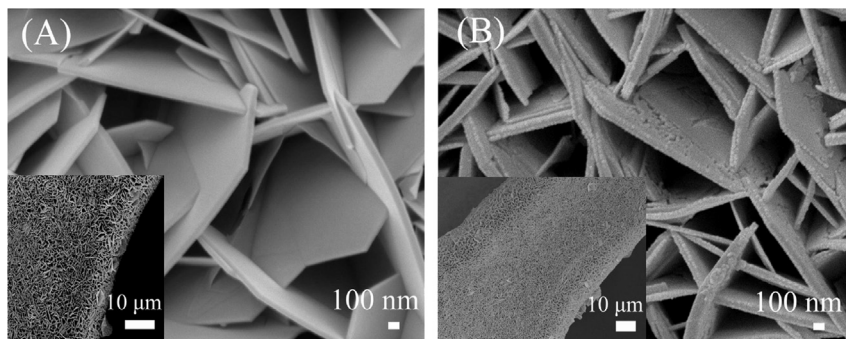
**Fig. 2.** SEM images of CoAl LDO NSA (A) and chemical etched $Co_3O_4$ NSA (B).

network and large "V-type" channels without collapse. Impressively, numerous holes of several to tens of nanometers in size can be easily found in the cross-linked nanosheets as compared with the intact CoAl LDO NSA. The large "V-type" channels combined with the holey structures can do benefit to the fully utilization of the active materials for high pseudo-capacitance, which will be discussed in the following section [52].

To demonstrate the validity of our synthesis strategy for constructing 3D core/shell hybrid nanostructures. The hydrothermal growing process of the $NiMoO_4$ shell was also studied by observing the morphologies along with the elongation of reaction time (0, 0.5, 1, and 2 h), as shown in Fig. 3. Before the hydrothermal reaction, the bare $Co_3O_4$-based NSA consists of regular nanosheets with numerous holes in them (Fig. 3A). After being immersed into the reaction solution and processed for 0.5 h, the sandwich-like nanostructures without spreading shell can be easily found (Fig. 3B). Impressively, the core/shell hierarchical nanostructures of $Co_3O_4@NiMoO_4$ NSA can be successfully formed under the hydrothermal growth time of 1 h (Fig. 3C). With prolonging the reaction time to 2 h, the $NiMoO_4$ shell has been completely coated on the surface of the $Co_3O_4$ NSA (Fig. 3D). Based on these results, the total

mass of the $NiMoO_4$ shell can be easily controlled via changing the hydrothermal growth time. Besides, the morphology changes of the hybrid electrodes along with the hydrothermal reaction time would play the key role in the capacitive performance undoubtedly, which will be confirmed in the following electrochemical characterizations.

The nanostructures of the bare $Co_3O_4$-based NSA and hybrid $Co_3O_4@NiMoO_4$ NSA (1 h sample) were further characterized by TEM, as shown in Fig. 4. In contrast to the bare $Co_3O_4$-based NSA (Fig. 4A), it can be found that a randomly oriented $NiMoO_4$ shell enwraps the $Co_3O_4$-based NSA (Fig. 4C), which is in good agreement with SEM observation. The high-resolution TEM (HRTEM) images of both samples are also shown in Fig. 4B and D. Thereinto, the HRTEM image of Fig. 4B shows an interplanar spacing of 0.241 nm, corresponding to the (311) planes of $Co_3O_4$. For the hybrid $Co_3O_4@NiMoO_4$ NSA (Fig. 4D), the lattice fringes with the spacing distances of 0.207 nm and 0.465 nm can be indexed to the (330) and (101) crystal planes of $NiMoO_4$ (JCPDS no. 33-0948), again demonstrating that the existence of α-$NiMoO_4$ in the hybrid sample.

To validate the advantages of our assistant synthesis method, we investigated the electrochemical performance of $Co_3O_4$-based NSA
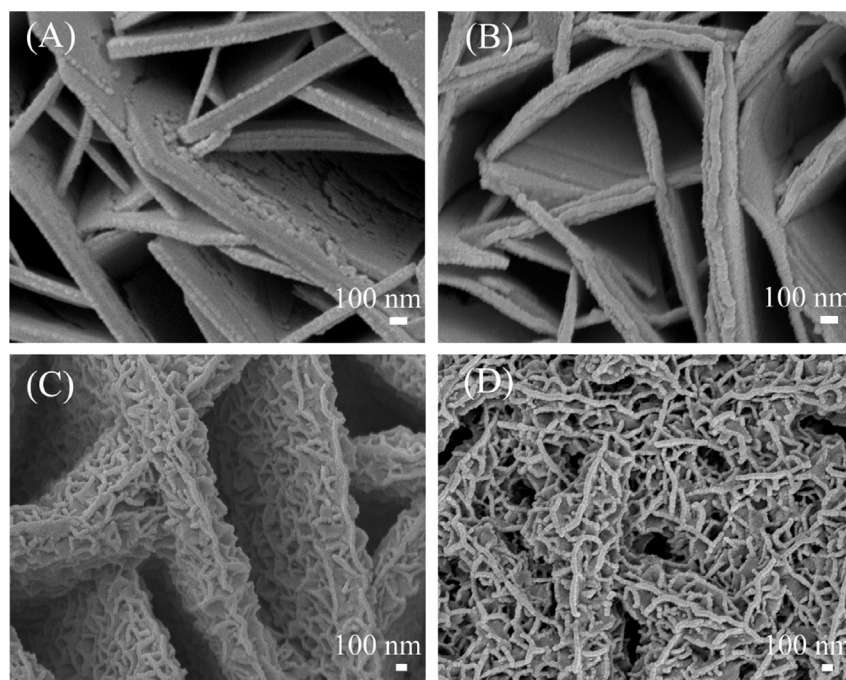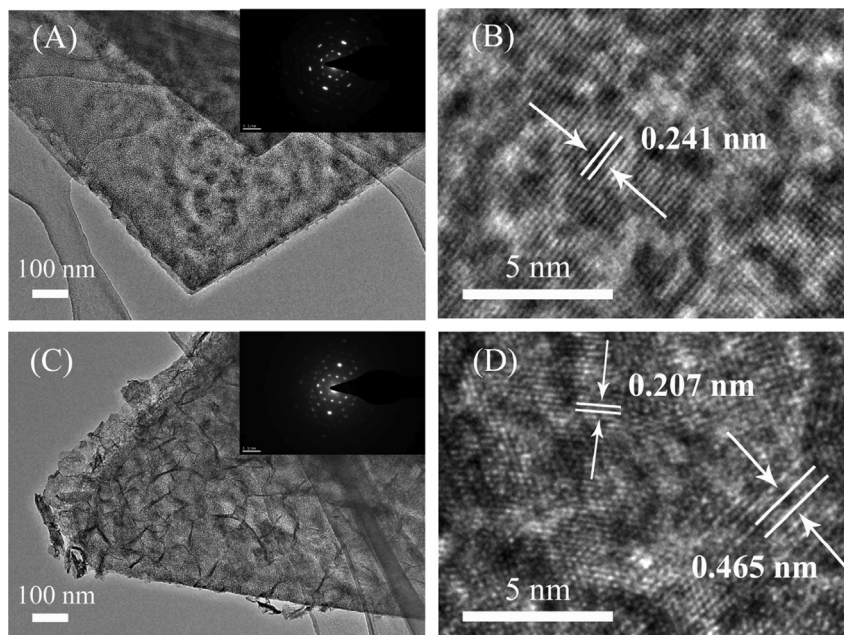


**Fig. 3.** SEM images of the electrodes obtained at different hydrothermal growth times: (A) 0 h, (B) 0.5 h, (C) 1 h, (D) 2 h.

**Fig. 4.** TEM and HRTEM images of chemical etched $Co_3O_4$ NSA (A, B) and hybrid $Co_3O_4@NiMoO_4$ NSA (C, D. 1 h sample). Inset: SAED patterns of chemical etched $Co_3O_4$ NSA (A) and hybrid $Co_3O_4@NiMoO_4$ NSA (C).

and CoAl LDO NSA in a preliminary study. As shown in Fig. 5, all measurements were carried out in a standard three-electrode cell with 2 M KOH aqueous solution as electrolyte. The typical cyclic voltammetry (CV) curves of the $Co_3O_4$-based NSA and CoAl LDO NSA electrodes within the potential window of $-0.2$–$0.6$ V (vs. SCE) at various scan rates are shown in Fig. 5A, C. In contrast to the CV curves of the CoAl LDO NSA, the $Co_3O_4$-based NSA has more distinct redox peaks. Besides, the enclosed CV curve area of the $Co_3O_4$-based NSA is obviously larger than that of the CoAl LDO NSA at the same scan rate (Fig. 5E), reflecting that the $Co_3O_4$-based NSA has higher specific capacitance [37]. This is in good agreement with the results obtained by the galvanostatic charge–discharge measurement (Fig. 5B, D). Based on the discharge curves of the two electrodes, the summary plots of the specific capacitances versus the current densities are shown in Fig. 5F. As can be seen, the specific capacitances of $Co_3O_4$-based NSA are calculated to be 1033 F g$^{-1}$ at a low current density of 3 mA cm$^{-2}$ (3.75 A g$^{-1}$) and 533 F g$^{-1}$ at a high current density of 30 mA cm$^{-2}$, and at least 51% level can be maintained, whereas the maximum specific capacitance of CoAl LDO NSA is only 516 F g$^{-1}$. In addition, the maximum specific capacitance reported here is much higher than those previously reported Co-based low dimensional building blocks, such as $Co_3O_4$ nanofilm (786 F g$^{-1}$ at 1 A g$^{-1}$) [25], $NiCo_2O_4$ nanowire (245 F g$^{-1}$ at 1 A g$^{-1}$) [37], $Co_3O_4$–NiO nanosheet (506 F g$^{-1}$ at 1 A g$^{-1}$) [56], $Co_3O_4$ porous nanowall (325 F g$^{-1}$ at 2 A g$^{-1}$) [57], porous $Co_3O_4$ nanofilm (443 F g$^{-1}$ at 2 A g$^{-1}$) [58], etc. Such enhanced pseudo-capacitive performance further proves the great advantages of the present chemical etching assistant method, which would make the $Co_3O_4$-based NSA more suitable as backbone for the subsequent construction of 3D hybrid electrode for supercapacitor applications.

To explore the potential of utilizing the hybrid $Co_3O_4@NiMoO_4$ in energy storage, similar electrochemical tests were also carried out on the hybrid electrodes with various hydrothermal growth times (Fig. 6). As can be seen, all the CV curves are consisted of two obvious redox peaks, indicating that the specific capacitance characteristics are mainly attributed to the faradic redox reactions of $Co^{3+}/Co^{4+}$ and $Ni^{2+}/Ni^{3+}$ (Fig. 6A, C and E) [13,40,59]. With the increase of the sweep rate, the anodic peak potential and cathodic peak potential shift to more anodic and cathodic directions, respectively. The galvanostatic discharge characteristics of different samples within a voltage range of 0–0.45 V are shown in Fig. 6B, D and F. It can be noted that the voltage plateaus match well with the peaks observed in the CV curve, and the nonlinear discharge curves further verify the pseudo-capacitive characteristics of hybrid $Co_3O_4@NiMoO_4$ electrodes. Based on the tests mentioned above, the electrochemical results of all samples were summarized for the following discussions. As shown in Fig. 7A, B, the specific capacitance values increase along with the hydrothermal growth time in a range of 0.5–1 h, and the sample with the growth time of 1 h presents the best electrochemical performance (1526 F g$^{-1}$ at 3 mA cm$^{-2}$). When the reaction time is further extended to 2 h, the total mass of the $NiMoO_4$ increases accordingly, whereas the maximum specific capacitance and the rate capability decrease. Thus the hydrothermal growth time of 1 h can be considered as the optimum choice for the construction of hybrid $Co_3O_4@NiMoO_4$ electrode in this case (Fig. 7C). As expected, the addition of $NiMoO_4$ not only offers another active material for capacitive reaction, but also provides an enlarged surface area of the whole electrode as the mass load increases. Based on the BET tests, the $Co_3O_4$-based NSA and hybrid $Co_3O_4@NiMoO_4$ NSA (sample of 1 h) have the specific surface areas of 5.98 m$^2$ g$^{-1}$ and 10.28 m$^2$ g$^{-1}$, respectively, whereas the specific area of the Ni foam substrate is only 0.13 m$^2$ g$^{-1}$ (Fig. S2, Table S1). The enlarged specific surface area of the binder-free electrode ensures sufficient exposure of the active materials to the KOH electrolyte. Moreover, the MSC and the ASC values of the bare $Co_3O_4$-based NSA and hybrid $Co_3O_4@NiMoO_4$ are also illustrated in Fig. 7D for comparison. The ASC values of hybrid $Co_3O_4@NiMoO_4$ are calculated to be 2.67, 2.58, 2.49, 2.35, 2.24, 2.12 and 1.92 F cm$^{-2}$ at current densities of 3, 5, 7, 10, 15, 20 and 30 mA cm$^{-2}$, respectively. The hybrid $Co_3O_4@NiMoO_4$ reserves 72% of its original capacitance when the current density is increased from 3 to 30 mA cm$^{-2}$, whereas the capacitance retention of the bare $Co_3O_4$-based NSA is about 51% (0.83 and 0.43 F cm$^{-2}$ at 3 and 30 mA cm$^{-2}$). Such enhanced performance suggests that the hybrid
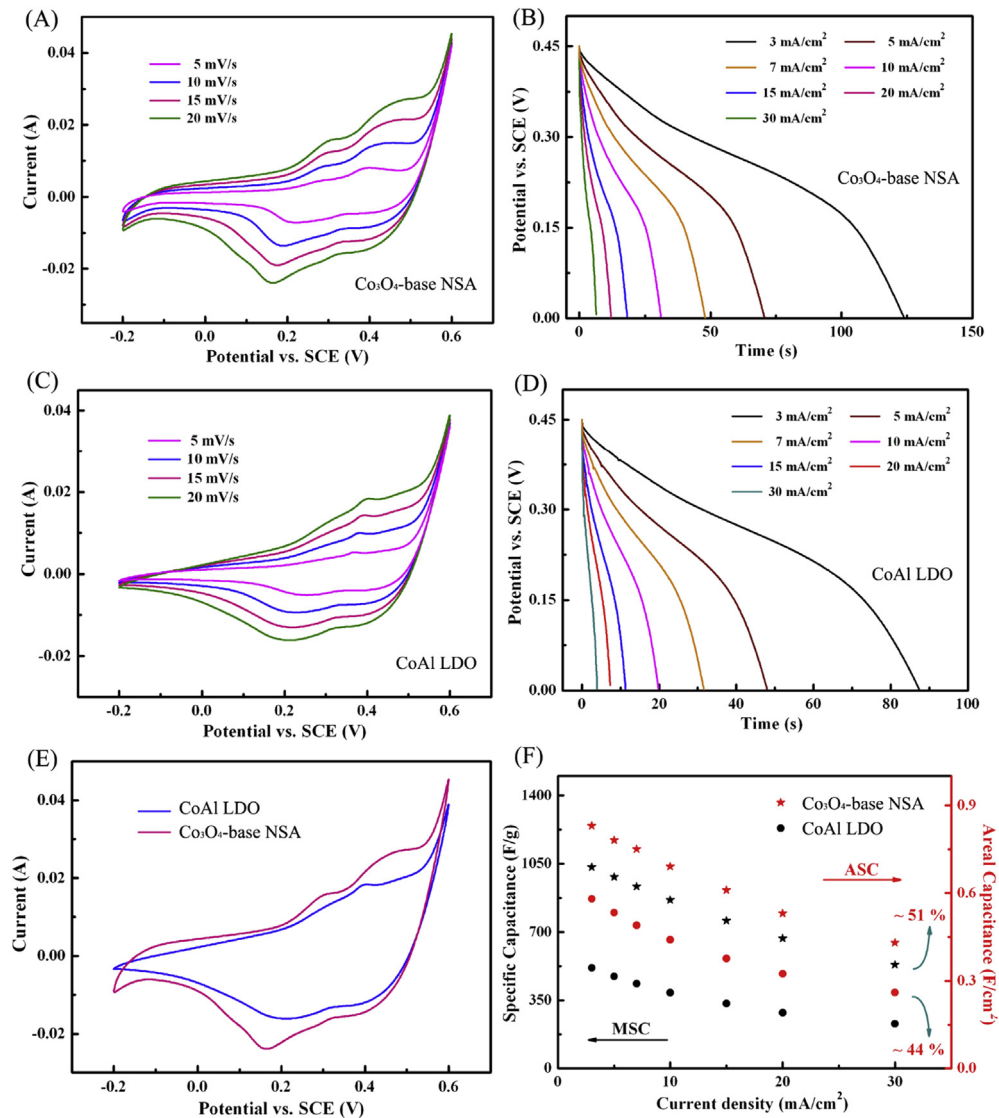
**Fig. 5.** Electrochemical performance of the bare $Co_3O_4$-based NSA (A, B) and the CoAl LDO NSA (C, D) electrodes measured in 2 M KOH solution. (A, C) CV curves of the bare $Co_3O_4$-based NSA and the CoAl LDO NSA electrodes at different scan rates, (B, D) discharge curves of the bare $Co_3O_4$-based NSA and the CoAl LDO NSA electrodes at different current densities, (E) CV curves of the bare $Co_3O_4$-based NSA and the CoAl LDO NSA electrodes at a scan rate of 20 mV s$^{-1}$, (F) Mass-specific capacitance and areal-specific capacitance of the bare $Co_3O_4$ NSA and the CoAl LDO NSA electrodes as a function of current densities.

electrode is more capable to maintain stable reactions with alkaline electrolyte at high current densities [20]. Besides, the capacitance values in this work are superior to those previously reported core/shell nanostructures, such as $Co_3O_4$@NiO nanowire arrays (1.35 F cm$^{-2}$ at 6 mA cm$^{-2}$) [60], $NiCo_2O_4$@$MnO_2$ nanowire arrays (2.244 F cm$^{-2}$ at 2 mA cm$^{-2}$) [61], $MnO_2$@NiO core/shell nanowire arrays (0.35 F cm$^{-2}$ at 9.5 mA cm$^{-2}$) [62], $NiCo_2O_4$@$NiCo_2O_4$ nanosheets array (2.20 F cm$^{-2}$ at 5 mA cm$^{-2}$) [24], and are also higher than those reported $AMoO_4$ (A = Co, Ni) based bulk materials, such as $CoMoO_4$/graphene (395 F g$^{-1}$ at 1 mV s$^{-1}$) [63], $NiMoO_4$ $x$H$_2$O nanorods (1136 F g$^{-1}$ at 5 mA cm$^{-2}$) [42], $NiMoO_4$ nanospheres (974 F g$^{-1}$ at 1 A g$^{-1}$) [38], Gr-$NiMoO_4$ $x$H$_2$O (367 F g$^{-1}$ at 5 A g$^{-1}$) [39], $CoMoO_4$–$NiMoO_4$ $x$H$_2$O bundles (1039 F g$^{-1}$ at 2.5 mA cm$^{-2}$) [43].

The electrochemical processes of these hybrid materials were further examined by EIS analysis, which were performed in a frequency range of 0.01–100 kHz at open circuit potential with an amplitude of 5 mV. As shown in Fig. 8, the X-intercept of the Nyquist plots in the high frequency range represents the equivalent

series resistance (ESR), which includes the ionic resistance of electrolyte, inherent resistances of the active material and contact resistance between electrolyte and electrode. Apparently, the sample of 1 h displays the smallest ESR, demonstrating that this hybrid electrode possesses the highest electrical conductivity. Besides, the Nyquist plot of 1 h sample also presents the smallest semicircle, indicating that it has a faster charge-transfer process than those of others. The above features are consistent with the higher capacitance and better capacitance retention of this sample as discussed in the preceding sections. Moreover, the 1 h sample has a more vertical line in the low frequency range, again validating its better capacitive behavior with lower diffusion resistance.

The cycling stability tests of the bare $Co_3O_4$-based NSA and hybrid $Co_3O_4$@$NiMoO_4$ NSA electrodes were carried out by using galvanostatic charge/discharge technique in the potential window of 0–0.45 V, as shown in Fig. 9. For the bare $Co_3O_4$-based NSA electrode, the ASC is about 0.72 F cm$^{-2}$ after 1000 cycles at the discharge current density of 7 mA cm$^{-2}$ (about 92% retention), indicating that the $Co_3O_4$-based NSA obtained through this
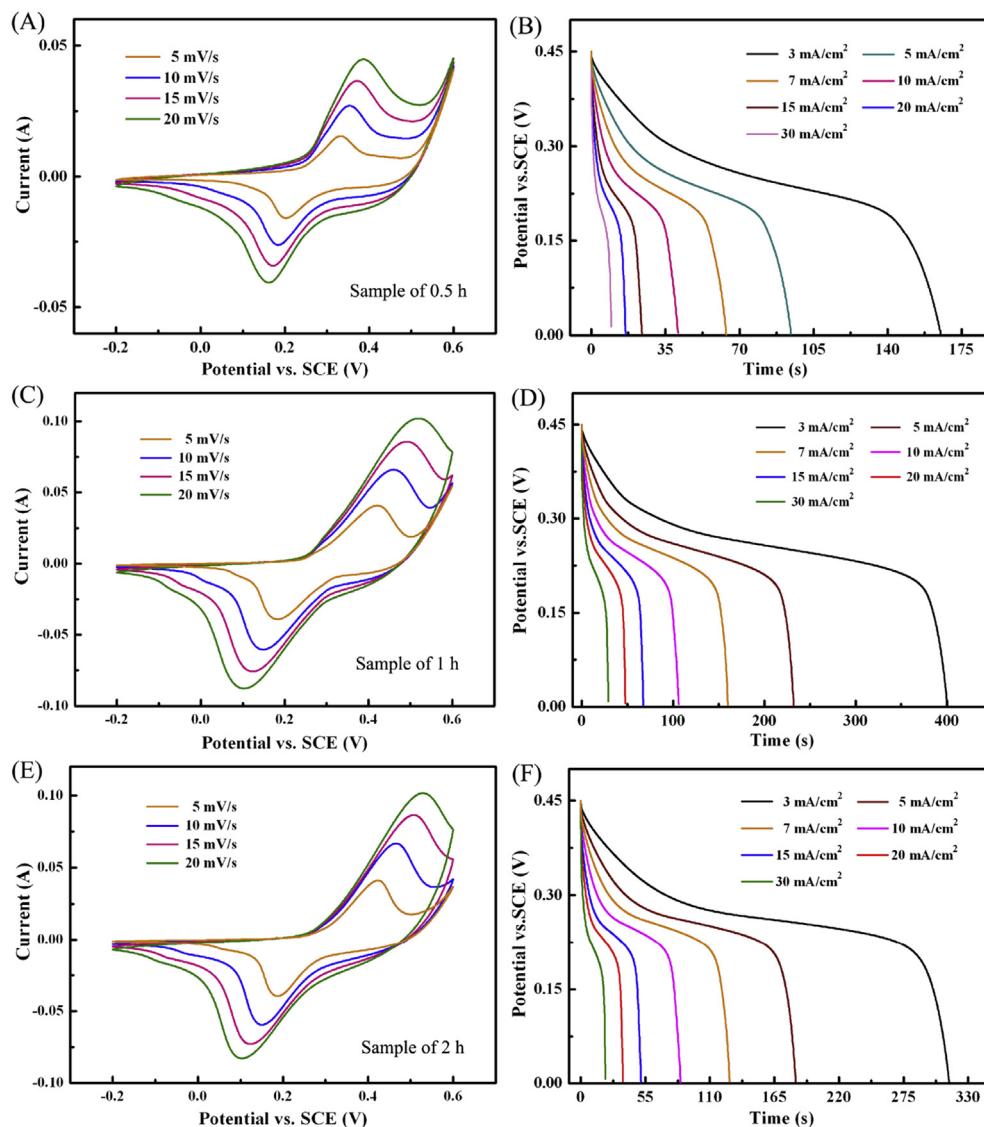
**Fig. 6.** Electrochemical performances of $Co_3O_4@NiMoO_4$ electrodes measured in 2 M KOH solution. (A, C, E) CV curves of $Co_3O_4@NiMoO_4$ electrodes at different scan rates, (B, D, F) discharge curves of $Co_3O_4@NiMoO_4$ electrodes at different current densities.

assistant method has the potential usage as 2D backbone for the construction of hybrid nanomaterials. Although, as the figure shows, the $Co_3O_4@NiMoO_4$ NSA electrode displays a declining behavior during such a long-term cycling tests (about 70% retention after 1000 cycles), the final ASC value is still better than that of the bare one even at a higher discharge current density of 15 mA cm$^{-2}$. This declining behavior is similar to those previously reported $AMoO_4$ (A = Co, Ni) based electrodes, which can be generally explained by the irreversible features of the Faraday reactions and the dissolution of active materials from the hybrid nanostructures during the cycling test [38,43,47,59].

To further explore the application of the hybrid $Co_3O_4@NiMoO_4$ nanostructures in EES, we used the as-synthesized $Co_3O_4@NiMoO_4$ NSA (sample of 1 h) as the positive electrode and activated carbon (AC) as the negative electrode to successfully fabricate an asymmetric supercapacitor ($Co_3O_4@NiMoO_4$ NSA//AC, Fig. 10). As can be seen, the potential windows of the $Co_3O_4@NiMoO_4$ NSA and AC electrodes are −0.2–0.6 V and −1.0 to 0 V, respectively. The CV curves of the AS at different scan voltage windows and different scan rates were also summarized, as illustrated in Fig. 10B, C. It

could be noted that the electrochemical windows of the AS can be extended to 1.6 V, and its CV curves reveal the contributions of both electric double layer capacitance and pseudo-capacitance. To obtain the specific capacitance, power density and energy density, the charge−discharge tests at different current densities were also carried out (Fig. 10D). Based on the calculated capacitance values, the as-fabricated $Co_3O_4@NiMoO_4$ NSA//AC asymmetric supercapacitor can deliver a maximum energy density of 37.8 Wh kg$^{-1}$ at a power density of 482 W kg$^{-1}$, and still retain 25.3 Wh kg$^{-1}$ at a high power density of 4819 W kg$^{-1}$ (Fig. 10E, F). The obtainable energy density values in this work are higher than those previously reported asymmetric supercapacitors with aqueous electrolytes, such as $NiCo_2O_4@MnO_2$//AC (35 Wh kg$^{-1}$) [61], Ni−Co binary hydroxides//CG (26.3 Wh kg$^{-1}$) [64], Ni−Co sulfides//AC (25 Wh kg$^{-1}$) [65] and GNCC//AC (7.6 Wh kg$^{-1}$) [66]. Moreover, we have assembled two supercapacitors in series and powered a 5 mm diameter red LED indicator, the corresponding photographs of the assembled system are shown in Fig. 11. All of these attractive results further demonstrate that the hybrid $Co_3O_4@NiMoO_4$ NSA have practical applications in EES.
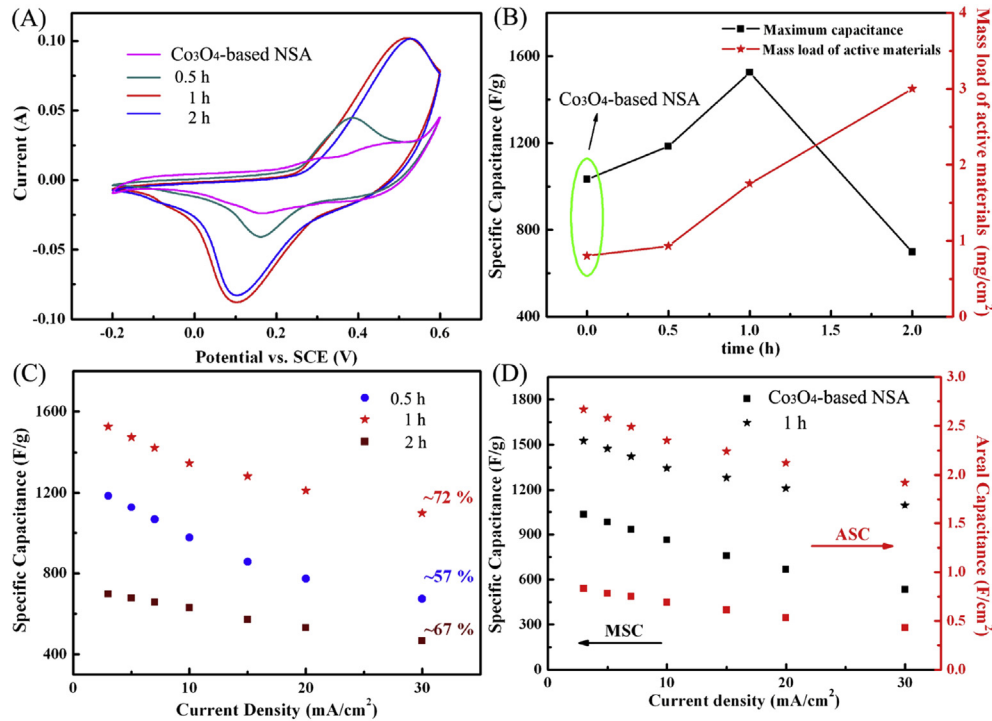
**Fig. 7.** (A) CV curves of the $Co_3O_4$ NSA and hybrid $Co_3O_4@NiMoO_4$ electrodes at a scan rate of 20 mV s$^{-1}$, (B) The specific capacitance values and mass load of active materials as a function of deposition time, (C) Specific capacitance of $Co_3O_4@NiMoO_4$ as function of current density, (D) Weight-specific capacitance and areal-specific capacitance of the bare $Co_3O_4$ NSA and hybrid $Co_3O_4@NiMoO_4$ electrodes as a function of current densities.

Based on the results mentioned above, the enhanced pseudo-capacitive performance of the hybrid $Co_3O_4@NiMoO_4$ electrode should be attributed to the outstanding structural features of each component. First, the porous $Co_3O_4$-based NSA obtained by chemical etching assistant approach can provide many "holes" in the uniform 2D structure. These holey nanosheets can expose a larger contact area to the electrolyte, thus the enhanced capacitive performance compared to the intact nanosheets array can be expected. Second, the hybrid nanostructures of $Co_3O_4@NiMoO_4$ increase the amount of accessible active sites for the capacitive reactions. On the one hand, the uniform 2D $Co_3O_4$-based building blocks can supply numerous large "V-type" channels between the

arrays, allowing full exposure of the nanosheets to the electrolyte. On the other hand, the loosely assembled $NiMoO_4$ obtained by hydrothermal synthesis is also beneficial for facilitating full contact of the $NiMoO_4$ shell with OH$^-$ in the electrolyte, which would improve the effective utilization of the active materials, and thus increasing the specific capacitance undoubtedly.

## 4. Conclusions

In summary, the uniform 2D $Co_3O_4$-based building blocks were successfully prepared through a facile and effective chemical
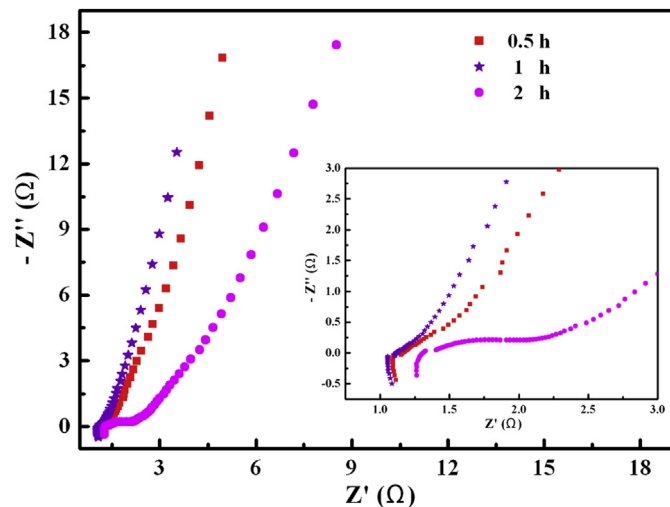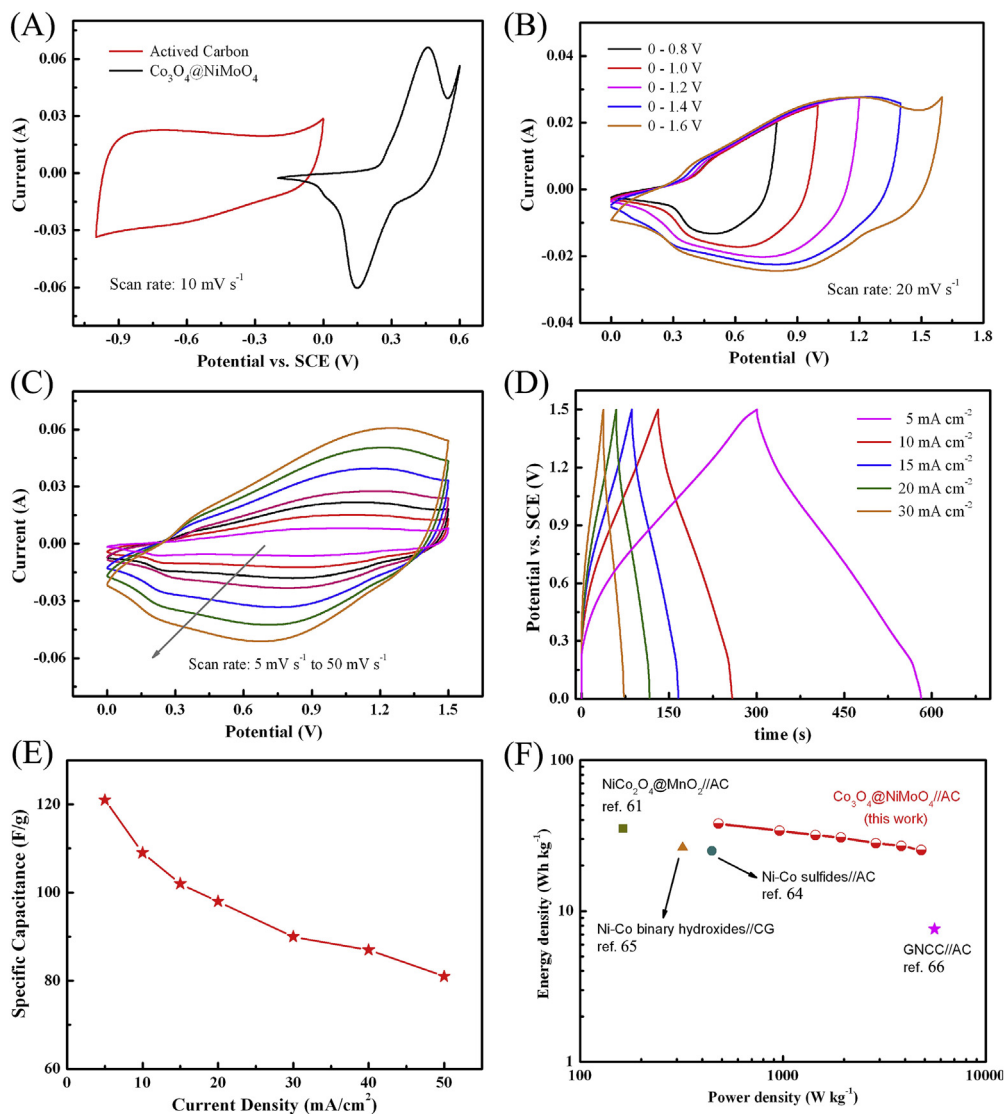


**Fig. 8.** EIS tests with the frequency from 0.01 Hz to 100 kHz. The inset shows the magnified high-frequency regions.
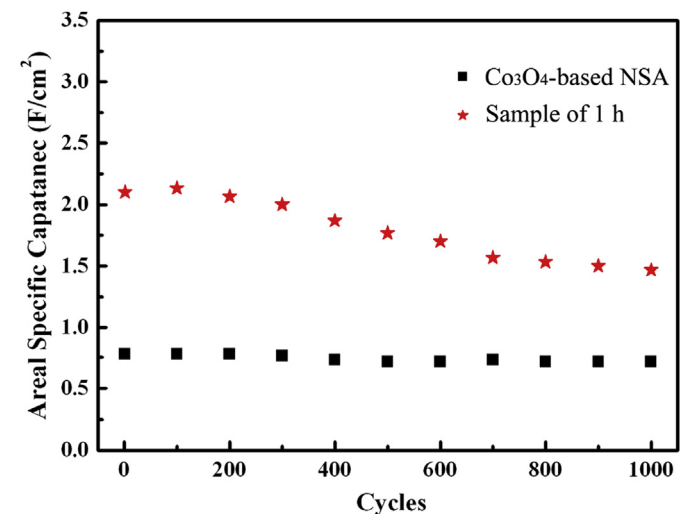


**Fig. 9.** The cycling stability tests of the bare $Co_3O_4$-based NSA and hybrid $Co_3O_4@Ni-MoO_4$ electrodes at different current densities (7 mA cm$^{-2}$ for the bare $Co_3O_4$-based NSA and 15 mA cm$^{-2}$ for the hybrid $Co_3O_4@NiMoO_4$).

**Fig. 10.** (A) CV curves of the hybrid $Co_3O_4@NiMoO_4$ (−0.2 to 0.6 V) and AC (−1.0 to 0 V) at a scan rate of 20 mV s$^{-1}$, (B, C) CV curves of the as-fabricated $Co_3O_4@NiMoO_4$//AC asymmetric supercapacitor at different scan voltage windows and different scan rates, respectively. (D) charge−discharge curves of the as-fabricated $Co_3O_4@NiMoO_4$//AC asymmetric supercapacitor at different current densities, (E) specific capacitance values of the $Co_3O_4@NiMoO_4$//AC asymmetric supercapacitor as function of current density, (F) Ragone plot of the $Co_3O_4@NiMoO_4$//AC asymmetric supercapacitor compared with other reported data.

etching assistant approach. The unique nanostructure shows the enhanced electrochemical behavior, which make it more suitable for constructing 3D hybrid electrode materials. As a binder-free electrode, the constructed 3D hybrid $Co_3O_4@NiMoO_4$ represents impressive pseudo-capacitive performances (a high specific capacitance of 1526 F g$^{-1}$ at a current density of 3 mA cm$^{-2}$ and a capacitance retention of 72%) as compared with the reported bulk $NiMoO_4$ based materials. Besides, an asymmetric supercapacitor
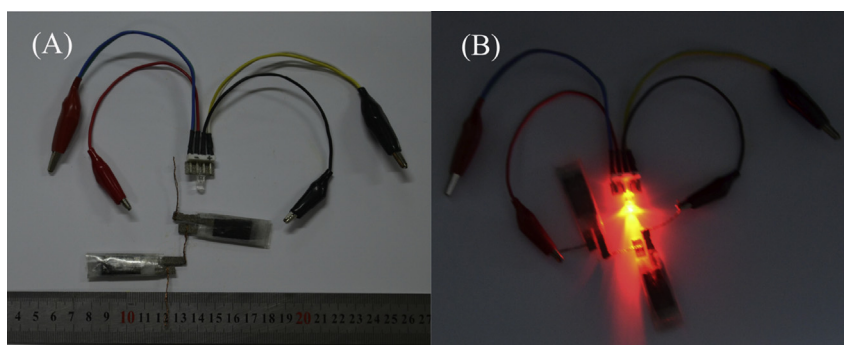


**Fig. 11.** (A) A photograph of the as-fabricated asymmetric supercapacitor devices and light-emitting diodes (LED), (B) A photograph of a red LED lighted up by two $Co_3O_4@NiMoO_4$//AC devices in series. (For interpretation of the references to color in this figure legend, the reader is referred to the web version of this article.)

based on this hybrid $Co_3O_4@NiMoO_4$ NSA and activated carbon can deliver a maximum energy density of 37.8 Wh $kg^{-1}$ at a power density of 482 W $kg^{-1}$. All these attractive results suggest that the aforementioned assistant synthesis strategy can be directly applied to other multifunctional components to construct 3D nano-structures, achieving the hybrid electrodes that hold the promise for practical applications in supercapacitor.

## Acknowledgments

## Appendix A. Supplementary data

Supplementary data related to this article can be found at http://dx.doi.org/10.1016/j.jpowsour.2014.07.149.

## References

[1] G. Wang, L. Zhang, J. Zhang, Chem. Soc. Rev. 41 (2012) 797–828.
[2] V. Augustyn, P. Simon, B. Dunn, Energy Environ. Sci. http://dx.doi.org/10.1039/c3ee44164d.
[3] H. Chen, L. Hu, M. Chen, Y. Yan, L. Wu, Adv. Funct. Mater. 24 (2014) 934–942.
[4] G. Zhang, X.W. Lou, Adv. Mater. 25 (2013) 976–979.
[5] G.X. Pan, X.H. Xia, F. Cao, P.S. Tang, H.F. Chen, Electrochem. Commun. 34 (2013) 146–149.
[6] F. Yang, J. Yao, F. Liu, H. He, M. Zhou, P. Xiao, Y. Zhang, J. Mater. Chem. A 1 (2013) 594–601.
[7] M. Shao, F. Ning, Y. Zhao, J. Zhao, M. Wei, D.G. Evans, X. Duan, Chem. Mater. 24 (2012) 1192–1197.
[8] B. Wang, Q. Liu, Z. Qian, X. Zhang, J. Wang, Z. Li, H. Yan, Z. Gao, F. Zhao, L. Liu, J. Power Sources 246 (2014) 747–753.
[9] Y. Zhao, Y. Meng, P. Jiang, J. Power Sources 259 (2014) 219–226.
[10] M. Yu, T. Zhai, X. Lu, X. Chen, S. Xie, W. Li, C. Liang, W. Zhao, L. Zhang, Y. Tong, J. Power Sources 239 (2013) 64–71.
[11] Q. Yang, Z. Lu, Z. Chang, W. Zhu, J. Sun, J. Liu, X. Sun, X. Duan, RSC Adv. 2 (2012) 1663–1668.
[12] Y. Tao, L. Zaijun, L. Ruiyi, N. Qi, K. Hui, N. Yulian, L. Junkang, J. Mater. Chem. 22 (2012) 23587–23592.
[13] J. Liu, J. Jiang, C. Cheng, H. Li, J. Zhang, H. Gong, H.J. Fan, Adv. Mater. 23 (2011) 2076–2081.
[14] L. Yang, S. Cheng, Y. Ding, X. Zhu, Z.L. Wang, M. Liu, Nano Lett. 12 (2012) 321–325.
[15] R.B. Rakhi, W. Chen, D. Cha, H.N. Alshareef, Nano Lett. 12 (2012) 2559–2567.
[16] X. Xia, J. Tu, Y. Zhang, J. Chen, X. Wang, C. Gu, C. Guan, J. Luo, H.J. Fan, Chem. Mater. 24 (2012) 3793–3799.
[17] C. Guan, X. Xia, N. Meng, Z. Zeng, X. Cao, C. Soci, H. Zhang, H.J. Fan, Energy Environ. Sci. 5 (2012) 9085–9090.
[18] Q. Li, Z.L. Wang, G.R. Li, R. Guo, L.X. Ding, Y.X. Tong, Nano Lett. 12 (2012) 3803–3807.
[19] M.J. Deng, P.J. Ho, C.Z. Song, S.A. Chen, J.F. Lee, J.M. Chen, K.T. Lu, Energy Environ. Sci. 6 (2013) 2178–2185.
[20] C. Guan, Z. Zeng, X. Li, X. Cao, Y. Fan, X. Xia, G. Pan, H. Zhang, H.J. Fan, Small 10 (2014) 300–307.
[21] W. Zhou, D. Kong, X. Jia, C. Ding, C. Cheng, G. Wen, J. Mater. Chem. A 2 (2014) 6310–6315.
[22] C. Guan, X. Li, Z. Wang, X. Cao, C. Soci, H. Zhang, H.J. Fan, Adv. Mater. 24 (2012) 4186–4190.
[23] Z. Lu, Q. Yang, W. Zhu, Z. Chang, J. Liu, X. Sun, D.G. Evans, X. Duan, Nano Res. 5 (2012) 369–378.
[24] X. Liu, S. Shi, Q. Xiong, L. Li, Y. Zhang, H. Tang, C. Gu, X. Wang, J. Tu, ACS Appl. Mater. Interfaces 5 (2013) 8790–8795.
[25] R.B. Rakhi, W. Chen, M.N. Hedhili, D. Cha, H.N. Alshareef, ACS Appl. Mater. Interfaces 6 (2014) 4196–4206.
[26] X.F. Lu, D.J. Wu, R.Z. Li, Q. Li, S.H. Ye, Y.X. Tong, G.R. Li, J. Mater. Chem. A 2 (2014) 4706.
[27] X. Xia, Z. Zeng, X. Li, Y. Zhang, J. Tu, N.C. Fan, H. Zhang, H.J. Fan, Nanoscale 5 (2013) 6040–6047.
[28] P.Y. Tang, Y.Q. Zhao, Y.M. Wang, C.L. Xu, Nanoscale 5 (2013) 8156–8163.
[29] W. Li, G. Li, J. Sun, R. Zou, K. Xu, Y. Sun, Z. Chen, J. Yang, J. Hu, Nanoscale 5 (2013) 2901–2908.
[30] D. Guo, H. Zhang, X. Yu, M. Zhang, P. Zhang, Q. Li, T. Wang, J. Mater. Chem. A 1 (2013) 7247–7254.
[31] C. Yuan, L. Yang, L. Hou, L. Shen, X. Zhang, X.W. Lou, Energy Environ. Sci. 5 (2012) 7883.
[32] C.W. Kung, H.W. Chen, C.Y. Lin, R. Vittal, K.C. Ho, J. Power Sources 214 (2012) 91–99.
[33] W. Hong, J. Wang, L. Niu, J. Sun, P. Gong, S. Yang, J. Alloys Compd. 608 (2014) 297–303.
[34] J. Li, W. Zhao, F. Huang, A. Manivannan, N. Wu, Nanoscale 3 (2011) 5103–5109.
[35] X. Wang, H. Liu, X. Chen, D.G. Evans, W. Yang, Electrochim. Acta 78 (2012) 115–121.
[36] M. Huang, F. Li, J.Y. Ji, Y.X. Zhang, X.L. Zhao, X. Gao, CrystEngComm 16 (2014) 2878–2884.
[37] H. Wang, X. Wang, ACS Appl. Mater. Interfaces 5 (2013) 6255–6260.
[38] D. Cai, D. Wang, B. Liu, Y. Wang, Y. Liu, L. Wang, H. Li, H. Huang, Q. Li, T. Wang, ACS Appl. Mater. Interfaces 5 (2013) 12905–12910.
[39] D. Ghosh, S. Giri, C.K. Das, Nanoscale 5 (2013) 10428–10437.
[40] D. Guo, P. Zhang, H. Zhang, X. Yu, J. Zhu, Q. Li, T. Wang, J. Mater. Chem. A 1 (2013) 9024–9027.
[41] D. Cai, B. Liu, D. Wang, Y. Liu, L. Wang, H. Li, Y. Wang, C. Wang, Q. Li, T. Wang, Electrochim. Acta 125 (2014) 294–301.
[42] M.C. Liu, L. Kang, L.B. Kong, C. Lu, X.J. Ma, X.M. Li, Y.C. Luo, RSC Adv. 3 (2013) 6472–6478.
[43] M.C. Liu, L.B. Kong, C. Lu, X.J. Ma, X.M. Li, Y.C. Luo, L. Kang, J. Mater. Chem. A 1 (2013) 1380–1387.
[44] B. Senthilkumar, D. Meyrick, Y.S. Lee, R.K. Selvan, RSC Adv. 3 (2013) 16542–16548.
[45] B. Senthilkumar, K. Vijaya Sankar, R. Kalai Selvan, M. Danielle, M. Manickam, RSC Adv. 3 (2013) 352–357.
[46] D. Cai, B. Liu, D. Wang, Y. Liu, L. Wang, H. Li, Y. Wang, C. Wang, Q. Li, T. Wang, Electrochim. Acta 115 (2014) 358–363.
[47] X.J. Ma, L.B. Kong, W.B. Zhang, M.C. Liu, Y.C. Luo, L. Kang, Electrochim. Acta 130 (2014) 660–669.
[48] D. Cai, D. Wang, B. Liu, L. Wang, Y. Liu, H. Li, Y. Wang, Q. Li, T. Wang, ACS Appl. Mater. Interfaces 6 (2014) 5050–5055.
[49] J. Han, Y. Dou, J. Zhao, M. Wei, D.G. Evans, X. Duan, Small 9 (2013) 98–106.
[50] J. Zhao, Z. Lu, M. Shao, D. Yan, M. Wei, D.G. Evans, X. Duan, RSC Adv. 3 (2013) 1045–1049.
[51] J. Zhao, M. Shao, D. Yan, S. Zhang, Z. Lu, Z. Li, X. Cao, B. Wang, M. Wei, D.G. Evans, X. Duan, J. Mater. Chem. A 1 (2013) 5840–5846.
[52] Z. Lu, W. Zhu, X. Lei, G.R. Williams, D. O'Hare, Z. Chang, X. Sun, X. Duan, Nanoscale 4 (2013) 3640–3643.
[53] W. Zhu, Z. Lu, G. Zhang, X. Lei, Z. Chang, J. Liu, X. Sun, J. Mater. Chem. A 1 (2013) 8327–8331.
[54] X.H. Xia, J.P. Tu, Y.J. Mai, X.L. Wang, C.D. Gu, X.B. Zhao, J. Mater. Chem. 21 (2011) 9319–9325.
[55] Y. Mi, Z. Huang, F. Hu, J. Jiang, Y. Li, Mater. Lett. 64 (2010) 695–697.
[56] X. Lu, X. Huang, S. Xie, T. Zhai, C. Wang, P. Zhang, M. Yu, W. Li, C. Liang, Y. Tong, J. Mater. Chem. 22 (2012) 13357–13364.
[57] J.B. Wu, Y. Lin, X.H. Xia, J.Y. Xu, Q.Y. Shi, Electrochim. Acta 56 (2011) 7163–7170.
[58] Y.F. Yuan, X.H. Xia, J.B. Wu, X.H. Huang, Y.B. Pei, J.L. Yang, S.Y. Guo, Electrochem. Commun. 13 (2011) 1123–1126.
[59] H. Zhang, Y. Chen, W. Wang, G. Zhang, M. Zhuo, H. Zhang, T. Yang, Q. Li, T. Wang, J. Mater. Chem. A 1 (2013) 8593–8600.
[60] X.H. Xia, J.P. Tu, Y.Q. Zhang, X.L. Wang, C.D. Gu, X.B. Zhao, H.J. Fan, ACS Nano 6 (2012) 5531–5538.
[61] K. Xu, W. Li, Q. Liu, B. Li, X. Liu, L. An, Z. Chen, R. Zou, J. Hu, J. Mater. Chem. A 2 (2014) 4795–4802.
[62] J. Liu, J. Jiang, M. Bosman, H.J. Fan, J. Mater. Chem. 22 (2012) 2419–2426.
[63] X. Xia, W. Lei, Q. Hao, W. Wang, X. Wang, Electrochim. Acta 99 (2013) 253–261.
[64] X. Sun, G. Wang, H. Sun, F. Lu, M. Yu, J. Lian, J. Power Sources 238 (2013) 150–156.
[65] Y. Li, L. Cao, L. Qiao, M. Zhou, Y. Yang, P. Xiao, Y. Zhang, J. Mater. Chem. A 2 (2014) 6540–6548.
[66] H. Wang, C. Holt, Z. Li, T. Xue, B. Amirkhiz, Z. Xu, B. Olsen, T. Stephenson, D. Mitlin, Nano Res. 5 (2012) 605–617.